



# Enhancing upconversion emissions of $\text{Er}^{3+}/\text{Tm}^{3+}/\text{Yb}^{3+}$ tridoped ( $\text{NaY}(\text{WO}_4)_2/\text{YF}_3$ ) through $\text{TiO}_2$ coating and $\text{Bi}^{3+}$ doping and its photocatalytic applications

Shouqiang Huang, Ziyang Lou, Zhibin Qi, Nanwen Zhu\*, Haiping Yuan

School of Environmental Science and Engineering, Shanghai Jiao Tong University, 800 Dongchuan Road, Shanghai 200240, PR China

## ARTICLE INFO

### Article history:

Received 2 November 2014

Received in revised form

20 December 2014

Accepted 23 December 2014

Available online 30 December 2014

### Keywords:

Photocatalyst

Near-infrared light

Upconversion

$\text{TiO}_2$  coating

$\text{Bi}^{3+}$  doping

## ABSTRACT

Enhanced upconversion property is important for the improvement of photocatalytic activity in the  $\text{TiO}_2$  based near-infrared (NIR) photocatalysts. Herein, an excellent NIR photocatalyst of  $\text{Er}^{3+}/\text{Tm}^{3+}/\text{Yb}^{3+}/\text{Bi}^{3+}$  doped ( $\text{NaY}(\text{WO}_4)_2/\text{TiO}_2/\text{YF}_3$ ) (ETYB-NTY) was synthesized with a multi-stage upconversion nanocrystal formation process. It is found that  $\text{TiO}_2$  coatings not only provide photocatalytic activity, but also improve the upconversion emission intensity, which is further enhanced greatly by the doped  $\text{Bi}^{3+}$  ions. Under NIR irradiations, ETYB-NTY possesses better photocatalytic activities compared to  $\text{Er}^{3+}/\text{Tm}^{3+}/\text{Yb}^{3+}$  doped ( $\text{NaY}(\text{WO}_4)_2/\text{TiO}_2/\text{YF}_3$ ) and  $\text{Er}^{3+}/\text{Tm}^{3+}/\text{Yb}^{3+}$  doped ( $\text{NaY}(\text{WO}_4)_2/\text{TiO}_2$ ), since more  $\cdot\text{OH}$  and  $\text{O}_2^{\cdot-}$  radicals can be produced by the much stronger UV (364 and 380 nm) and violet (409 nm) upconversion emissions in ETYB-NTY. There are also clear improvements for ETYB-NTY in degradation of methyl orange, salicylic acid, and the leachate from incineration plant under UV–vis–NIR irradiation. ETYB-NTY is a novel NIR photocatalyst with special structure and enhanced upconversion property, which has promising applications in organic pollution treatment and solar energy utilization.

© 2014 Elsevier B.V. All rights reserved.

## 1. Introduction

Near-infrared (NIR) responsive photocatalytic activity based on upconversion has aroused wide attention due to the utilization of NIR light occupied ~44% in the solar spectrum. To obtain high upconversion efficiencies, the most efficient host materials, i.e.,  $\text{NaYF}_4$  [1],  $\text{YF}_3$  [2],  $\text{LaF}_3$  [3], and  $\text{CaF}_2$  [4] have been used. Meanwhile,  $\text{TiO}_2$  is the most commonly used semiconductor in the fabrication of NIR photocatalysts [1–3]. However, the upconversion emission intensities are often decreased in the  $\text{TiO}_2$  coated NIR photocatalysts compared to their pure upconversion agents, owing to the light-scattering caused by the  $\text{TiO}_2$  shells, and the final photocatalytic activities are weakened. Having these in mind, it inspired us to fabricate the NIR photocatalyst, whose upconversion properties and photocatalytic activities can both be improved by  $\text{TiO}_2$  itself and some adding dopants.

Until now, very limited work has been focused on the enhancement of upconversion by combining with anatase- $\text{TiO}_2$ . Recently, a novel composite of  $\text{TiO}_2$  inverse opal/ $\text{NaYF}_4$ :  $\text{Tm}^{3+}$ ,  $\text{Yb}^{3+}$  was reported by Xu et al. [5], and its overall upconversion emission

intensity was about 43 times higher than that of pure  $\text{NaYF}_4$ :  $\text{Tm}^{3+}$ ,  $\text{Yb}^{3+}$ . They confirmed that the multi-layer structure of  $\text{TiO}_2$  inverse opal was favorable for the modulation of the upconversion process. Furthermore, a multi-stage formation of upconversion agents can be utilized to synthesize the NIR photocatalysts [6], where a precursor with low solubility product can slowly release  $\text{Ca}^{2+}$  ions into a solution containing  $\text{F}^-$  ions to form upconversion nanocrystals. At the same time,  $\text{TiO}_2$  nanocrystals would deposit continuously on the precursor and separate well the upconversion nanocrystals. Thus, a multi-layer structure consisted of  $\text{TiO}_2$  and upconversion nanocrystals could be built on the remaining precursor. Benefit from this special structure, the upconversion property can be improved.

In this work, a double alkaline rare-earth tungstate of  $\text{NaY}(\text{WO}_4)_2$  was used as the precursor to slowly release  $\text{Y}^{3+}$  ions. With the addition of titanium isopropoxide and NaF, a novel NIR photocatalyst of  $\text{Er}^{3+}/\text{Tm}^{3+}/\text{Yb}^{3+}$  doped ( $\text{NaY}(\text{WO}_4)_2/\text{TiO}_2/\text{YF}_3$ ) (ETY-NTY) was fabricated following a hydrothermal method. Meanwhile, it was reported that  $\text{Bi}^{3+}$  ions can not only enhance the upconversion properties [4,7], but also improve the photocatalytic activities of  $\text{TiO}_2$  [8]. Therefore, an excellent NIR photocatalyst of  $\text{Er}^{3+}/\text{Tm}^{3+}/\text{Yb}^{3+}/\text{Bi}^{3+}$  doped ( $\text{NaY}(\text{WO}_4)_2/\text{TiO}_2/\text{YF}_3$ ) (ETYB-NTY) was further fabricated. For the comparison of structures, morphologies, and upconversion properties,  $\text{Er}^{3+}/\text{Tm}^{3+}/\text{Yb}^{3+}$  doped

\* Corresponding author. Tel.: +86 21 54743710; fax: +86 21 54743710.

E-mail address: [nwzhu@sjtu.edu.cn](mailto:nwzhu@sjtu.edu.cn) (N. Zhu).

$\text{NaY}(\text{WO}_4)_2$  (ETY-N),  $\text{Er}^{3+}/\text{Tm}^{3+}/\text{Yb}^{3+}$  doped ( $\text{NaY}(\text{WO}_4)_2/\text{YF}_3$ ) (ETY-NY),  $\text{Er}^{3+}/\text{Tm}^{3+}/\text{Yb}^{3+}/\text{Bi}^{3+}$  doped ( $\text{NaY}(\text{WO}_4)_2/\text{YF}_3$ ) (ETYB-NY), and  $\text{Er}^{3+}/\text{Tm}^{3+}/\text{Yb}^{3+}$  doped ( $\text{NaY}(\text{WO}_4)_2/\text{TiO}_2$ ) (ETY-NT) were also synthesized. The photocatalytic activities of the samples were evaluated by the degradation of methyl orange (MO), salicylic acid (SA), and the leachate under NIR and UV–vis–NIR irradiations. The three dimensional excitation–emission matrix spectra were also used to investigate the degradation processes.

## 2. Experimental methods

### 2.1. Chemicals and materials

$\text{Y}(\text{NO}_3)_3 \cdot 6\text{H}_2\text{O}$ ,  $\text{Na}_2\text{WO}_4 \cdot 2\text{H}_2\text{O}$ ,  $\text{Er}(\text{NO}_3)_3 \cdot 5\text{H}_2\text{O}$ ,  $\text{Tm}(\text{NO}_3)_3 \cdot 5\text{H}_2\text{O}$ ,  $\text{Yb}(\text{NO}_3)_3 \cdot 5\text{H}_2\text{O}$ ,  $\text{Bi}(\text{NO}_3)_3 \cdot 5\text{H}_2\text{O}$ , and titanium isopropoxide (TTIP, 98%) were used as received without further purification.

### 2.2. Preparation of the $\text{NaY}(\text{WO}_4)_2$ precursors

6 mmol  $\text{Na}_2\text{WO}_4 \cdot 2\text{H}_2\text{O}$  was dissolved into 50 mL of distilled water, and then added dropwise into an aqueous solution containing 50 mL of  $\text{Y}(\text{NO}_3)_3 \cdot 6\text{H}_2\text{O}$  (0.2 M) under continuous stirring for 2 h. The obtained precipitation through centrifugation and washing were dried at 60 °C for 12 h.

### 2.3. Preparation of the ETYB-NTY samples

In a typical procedure for ETYB-NTY,  $\text{NaY}(\text{WO}_4)_2$ ,  $\text{Er}(\text{NO}_3)_3 \cdot 5\text{H}_2\text{O}$ ,  $\text{Tm}(\text{NO}_3)_3 \cdot 5\text{H}_2\text{O}$ ,  $\text{Yb}(\text{NO}_3)_3 \cdot 5\text{H}_2\text{O}$  and  $\text{Bi}(\text{NO}_3)_3 \cdot 5\text{H}_2\text{O}$  were added into 40 mL of distilled water and totally dispersed by ultrasonication, and the pH of the mixture was adjusted to 1 by adding nitric acid. Then, 20 mL of absolute ethanol containing 2 mmol of TTIP was added dropwise into the above mixture. The molar ratio of  $\text{Ti}^{4+}:\text{Y}^{3+}:\text{Yb}^{3+}:\text{Er}^{3+}:\text{Tm}^{3+}:\text{Bi}^{3+}$  was 100%:30%:20%:2%:2%:2%. After stirring for 30 min, 40 mL of aqueous solution containing 7 mmol NaF was introduced into the mixture (Fig. 1). The resulted mixture was transferred into a 150 mL Teflon-lined stainless steel autoclave, and heated at 180 °C for 12 h. The precipitates after centrifugation, washing and drying were heated at 500 °C for 4 h to obtain the ETYB-NTY samples.

Meanwhile, ETY-N, ETY-NY, ETYB-NY, ETY-NT, and ETY-NTY were also fabricated following the procedures mentioned above.

### 2.4. Characterization

X-ray power diffraction (XRD) was performed on a Bruker D8 Advance X-ray Diffractometer at 40 kV and 40 mA using  $\text{Cu K}\alpha$  radiation ( $\lambda = 1.5406 \text{ \AA}$ ). The morphologies were observed by means of the Sirion 200 field emission scanning electron microscope (FESEM) and the JEM-2100F transmission electron microscope (TEM). The absorption spectra were carried out on the Lambda 750 UV–vis–NIR (UV–vis–Near Infrared) spectrophotometer. Room temperature upconversion fluorescence spectra and photoluminescence (PL) spectra were measured by a Hitachi F-7000 fluorescence spectrophotometer equipped with a 980 nm semiconductor solid laser with tunable power. For lifetime measurements, a Raman shift laser running at 953.6 nm was generated by the second-order Stokes stimulated Raman scattering of hydrogen under the excitation of the 532 nm line of a Nd:YAG pulsed laser (Quantum-Ray). The electron spin resonance (ESR) spectra were recorded on an EMX-8 ESR spectrometer (Bruker BioSpin Corp.) with a microwave power of 5 mW.

### 2.5. Photocatalytic activities

The photocatalytic activities of the samples were evaluated by the degradation of MO and SA under 980 nm, NIR ( $\lambda \geq 780 \text{ nm}$ ) and UV–vis–NIR (provided by a 1000 W high pressure mercury lamp with a filter) light irradiations. 20 mL of MO or SA aqueous solutions (10 mg/L) were placed in the quartz glass tubes, and then 20 mg of the samples were added. Prior to irradiation, the suspensions were magnetically stirring in the dark for 2 h to reach adsorption/desorption equilibrium. Every periodic interval, 2.0 mL of the suspensions were collected and centrifuged, and then detected by a UV–vis spectrophotometer (Hitachi U-3900). The  $\cdot\text{OH}$  and  $\text{O}_2^{\cdot-}$  radicals generated from the samples were determined by terephthalic acid (TA,  $4 \times 10^{-4} \text{ M}$  in a  $2 \times 10^{-3} \text{ M}$  NaOH) and Nitroblue tetrazolium (NBT,  $1 \times 10^{-3} \text{ M}$ ) solutions, respectively, where the test methods were similar to those for the MO and SA degradations. Leachate collected from Shanghai Laogang refuse incineration plant was also used to test the photocatalytic activity of ETYB-NTY,

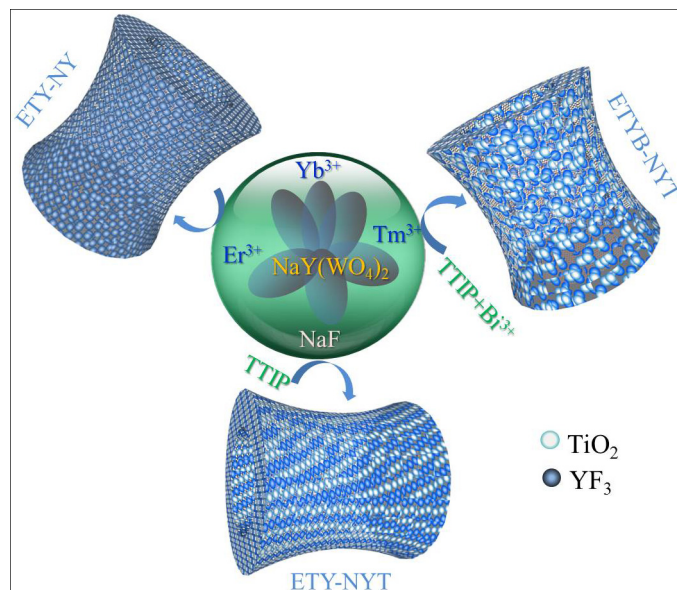


Fig. 1. Schematic illustrations for the multi-stage formation of ETY-NY, ETY-NTY, and ETYB-NTY.

where the corresponding total organic carbon (TOC) and pH was 19,090 mg/L and 6.26, respectively. The leachate was diluted 50 times, and then the UV–vis–NIR irradiated leachate samples were characterized by fluorescence excitation–emission matrix (EEM) spectroscopy (F-7000, Hitachi). Scanning emission spectra were obtained from 250 to 600 nm by varying the excitation wavelength from 200 to 400 nm at 5 nm increments. 1.0 mL of the leachate samples were also diluted 25 times for the TOC measurements by a multi N/C 3100 analyzer (Analytik Jena AG, Jena, Germany).

### 3. Results and discussion

#### 3.1. Characterization of the samples

The XRD patterns of the samples are shown in Fig. 2. ETY-NT contains two phases of  $\text{NaY}(\text{WO}_4)_2$  (JCPDS Card No. 48-0886) and anatase- $\text{TiO}_2$  (JCPDS Card No. 71-1166) (Fig. 2a). With the addition of NaF, the cations ( $\text{Na}^+$  or  $\text{Y}^{3+}$ ) in  $\text{NaY}(\text{WO}_4)_2$  will be slowly taken by  $\text{F}^-$  ions, due to the different solubility products, which can produce some fluoride compounds. As shown in the XRD pattern of ETY-NY (Fig. 2b), except for  $\text{NaY}(\text{WO}_4)_2$ , the main diffraction peaks at  $24.56^\circ$ ,  $26.08^\circ$ ,  $27.86^\circ$ , and  $47.18^\circ$  are assigned to the (1 0 1), (0 2 0), (1 1 1), and (1 3 1) planes of  $\text{YF}_3$  (JCPDS Card No. 74-0911), respectively. In particular, some weak  $\text{NaYF}_4$  related peaks are found at  $28.25^\circ$ ,  $47.18^\circ$ ,  $55.81^\circ$ , and  $58.45^\circ$ , which correspond to the (1 1 1), (2 2 0), (3 1 1), and (2 2 2) planes of  $\text{NaYF}_4$  (JCPDS Card No. 77-2042), respectively. Thus, the obtained fluorides of  $\text{YF}_3$  and  $\text{NaYF}_4$  can be the excellent mixed host materials for  $\text{Er}^{3+}/\text{Tm}^{3+}/\text{Yb}^{3+}$  ions. The diffraction peaks of ETY-NTY (Fig. 2c) are broadened owing to the combined  $\text{TiO}_2$  nanocrystals with an average size of 15.79 nm (Table S1). After doping with  $\text{Bi}^{3+}$  ions, the diffraction peak intensities possess a certain degree of enhancement for ETYB-NTY (Fig. 2d) compared to ETY-NTY, meaning the increased crystallinity is displayed by the doped  $\text{Bi}^{3+}$  ions. It can be found that the lattice parameters of  $\text{YF}_3$  (JCPDS Card No. 32-1431) are changed slightly, with a higher cell volume of  $191.69 \text{ \AA}^3$  compared to that ( $191.17 \text{ \AA}^3$ ) of ETY-NTY and ETY-NY (Table S2), indicating that the  $\text{Y}^{3+}$  ions ( $0.89 \text{ \AA}$ ) in  $\text{YF}_3$  are partially substituted by  $\text{Bi}^{3+}$  ions with larger ionic radius ( $0.96 \text{ \AA}$ ) [8].

The morphology of ETY-NYT (Fig. 3a, S1d, and S2c) possesses many regular microrod crystals, which are uniformly coated by  $\text{TiO}_2$  nanoparticles. It can be clearly observed that many nanopores exist in the surfaces of the microrod crystals, and they are the diffusion channels formed by the  $\text{Y}^{3+}$  ion diffusions from the inner  $\text{NaY}(\text{WO}_4)_2$  cores to the solid–liquid interfaces. As seen in Fig. 3b and c and S1e, ETYB-NTY also displays microrod morphologies with porous structure, while its coating surfaces become coarse and thicker compared to those of ETY-NTY. From the high-resolution TEM (HRTEM) images (Fig. 3d and f), it can be found that  $\text{YF}_3$  and  $\text{TiO}_2$  nanocrystals are present in the outmost surface of ETYB-NTY, and both of them have clear lattice fringes, indicating their high crystallinity. The Fourier-transform electron diffraction pattern of  $\text{YF}_3$  crystal confirms its preferential  $[10\bar{1}]$  growth direction (inset of Fig. 3d). Thus, the obtained  $\text{YF}_3$  nanocrystals are not completely coated by  $\text{TiO}_2$ , and they are connected to each other (Fig. 3e).

#### 3.2. Optical properties

Fig. 4a shows the upconversion luminescence spectra of ETY-N, ETY-NT, ETY-NY, ETYB-NY, ETY-NTY, and ETYB-NTY under 980 nm NIR light excitation. The blue (474 nm) and green (522 and 545 nm) light emissions are attributed to the transitions of  $^1\text{G}_4 \rightarrow ^3\text{H}_6$  ( $\text{Tm}^{3+}$ ),  $^2\text{H}_{11/2} \rightarrow ^4\text{I}_{15/2}$  ( $\text{Er}^{3+}$ ), and  $^4\text{S}_{3/2} \rightarrow ^4\text{I}_{15/2}$  ( $\text{Er}^{3+}$ ), respectively. Other emissions include the red (658 nm), violet (409 nm), and UV (364 and 380 nm) light. It is interesting to observe that ETY-NTY

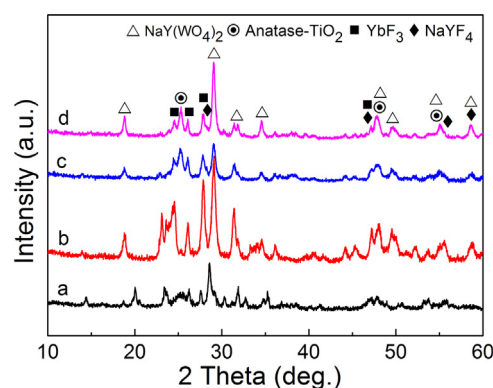


Fig. 2. XRD patterns of (a) ETY-NT, (b) ETY-NY, (c) ETY-NTY, and (d) ETYB-NTY.

possesses higher emission intensities than the  $\text{TiO}_2$  free sample of ETY-NY, and the upconversion emissions are further enhanced greatly by  $\text{Bi}^{3+}$  doping in ETYB-NTY (Fig. S3 and S4). It is worth noting that the maximum blue emission intensities of ETY-NTY and ETYB-NTY are about 3 and 21 times higher than that of ETY-NY, respectively. Thus, the anatase- $\text{TiO}_2$  coatings are not detrimental for the excitation. Instead, the upconversion emission intensities are enhanced by  $\text{TiO}_2$  in the multi-stage formed samples of ETY-NTY and ETYB-NTY.

It was reported that the non-crystalline  $\text{TiO}_2$  coating could improve the upconversion emissions of  $\text{Tm}^{3+}/\text{Yb}^{3+}-\text{Y}_2\text{O}_3$  [9]. Nevertheless, for many anatase- $\text{TiO}_2$  based NIR photocatalysts [1–3], the upconversion enhancement was not present, and it is associated with many factors, such as the thickness and the different polymorphs of  $\text{TiO}_2$  shells. Particularly, Xu et al. have found the upconversion properties could be improved by  $\text{TiO}_2$  inverse opals with multi-layer structure [5]. In comparison to the single  $\text{YF}_3$  contained surface layer of ETY-NY, the mixed phases of  $\text{TiO}_2$  and  $\text{YF}_3$  are included for ETY-NTY and ETYB-NTY. According to the TEM images of ETYB-NTY, it is important to find that the  $\text{TiO}_2$  and  $\text{YF}_3$  nanocrystals are connected to each other. Meanwhile, ETY-NTY and ETYB-NTY also have the multi-layer structures, since  $\text{YF}_3$  nanocrystals are formed continuously during the whole hydrothermal reaction processes. From Fig. S5a and b, it can be found that the upconversion emission intensities of ETYB-NTY are enhanced gradually as the hydrothermal time extended, which are resulted from the increased amount of  $\text{YF}_3$  crystals and the higher crystallinity. The time behaviors of the  $^2\text{H}_{11/2} \rightarrow ^4\text{I}_{15/2}$  ( $\text{Er}^{3+}$ ) and  $^1\text{G}_4 \rightarrow ^3\text{H}_6$  ( $\text{Tm}^{3+}$ ) transitions for ETY-NY, ETY-NTY, and ETYB-NTY are shown in Fig. 4c and d, respectively. All the decay curves can be fitted well to a single exponential function and the lifetimes are obtained from least square analysis [10]. After coating with  $\text{TiO}_2$ , the decay curves of ETY-NTY have been shifted, and its lifetimes of the  $^2\text{H}_{11/2}$  and  $^1\text{G}_4$  levels are increased to 163 and 183  $\mu\text{s}$ , longer than those (160 and 174  $\mu\text{s}$ ) of ETY-NY, respectively, meaning that the surface-quenching effect in ETY-NTY have been suppressed [11]. The reasonable explanation is related to the decreased surface defects modulated by  $\text{TiO}_2$  coatings, since a larger lattice mismatch between  $\text{NaY}(\text{WO}_4)_2$  and  $\text{YF}_3$  can be formed compared to that obtained between  $\text{NaY}(\text{WO}_4)_2$  and  $\text{TiO}_2$  (Table S2).

In the present case of ETYB-NTY, the host crystal field has been modified by  $\text{Bi}^{3+}$  ions due to the slight increased cell volume of  $\text{YF}_3$ . ETYB-NTY also possesses higher crystallinity and less surface defects compared to ETY-NTY. Moreover, there is an increase in the lifetimes of the  $^2\text{H}_{11/2}$  (164  $\mu\text{s}$ ) and  $^1\text{G}_4$  (180  $\mu\text{s}$ ) levels. Thus, the radiative transition rates can be increased, which results in much enhanced upconversion emission intensities for ETYB-NTY. It is conceivable that the energy transfer processes from  $\text{Yb}^{3+}$  to  $\text{Er}^{3+}$  and  $\text{Tm}^{3+}$  will not be changed by the doped  $\text{Bi}^{3+}$  ions, while the



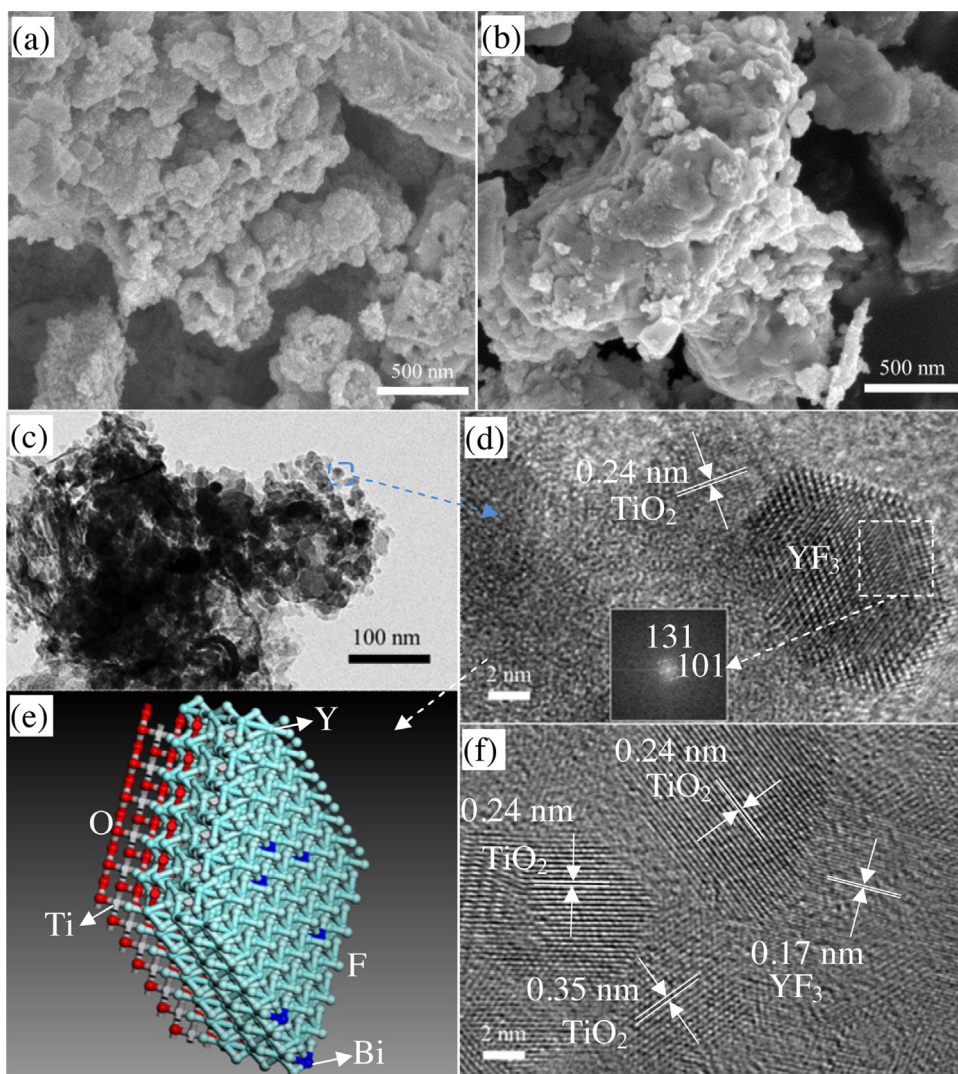


**Fig. 3.** SEM images of (a) ETY-NYT and (b) ETYB-NYT. (c) TEM and (d and f) HRTEM images (inset: Fourier transform electron diffraction pattern) of ETYB-NYT. (e) Schematic illustration of the connected  $\text{YF}_3$  and  $\text{TiO}_2$  nanocrystals, and the substitution of  $\text{Y}^{3+}$  ions by  $\text{Bi}^{3+}$  ions.

local crystal field of the host lattice has been tailored by  $\text{Bi}^{3+}$  ions to enlarge the lifetimes of the intermediate levels of lanthanide ions through changing their wave functions [7,12]. It should be noted that the dramatic enhancement of upconversion emissions in ETYB-NYT by  $\text{Bi}^{3+}$  doping is based on the  $\text{TiO}_2$  coatings. In the  $\text{TiO}_2$  free sample of ETYB-NY (Fig. S3 and S4), the upconversion improvement by  $\text{Bi}^{3+}$  doping is not remarkable, and it is another factor to demonstrate the significant role of  $\text{TiO}_2$  displayed in the modulation of the upconversion emission process.

As seen in Fig. S5c, the upconversion emission intensities are firstly increased and then decreased as the  $\text{Bi}^{3+}$  doping contents increased, since the distances between  $\text{Yb}^{3+}$ ,  $\text{Er}^{3+}$  and  $\text{Tm}^{3+}$  will be enlarged by the excess doping concentration of  $\text{Bi}^{3+}$  ions, and the energy transfer from  $\text{Yb}^{3+}$  to  $\text{Er}^{3+}$  and  $\text{Tm}^{3+}$  ions will become difficult. There is an optimal doping concentration of  $\text{Bi}^{3+}$  ions to obtain the strongest upconversion luminescence. The UV–vis–NIR absorption properties of the samples are shown in Fig. 4e and f, and the band gap energy of ETYB-NYT is calculated to be 2.88 eV (431 nm) (Table S1). Hamdi et al. reported that the absorption edge of  $\text{TiO}_2$  could be enlarged to 570 nm by doping with 3%  $\text{Bi}^{3+}$  ions [8]. Nevertheless, the extended absorption edge is not observed in ETYB-NYT with 2%  $\text{Bi}^{3+}$  ions, and it is due to the low  $\text{Bi}^{3+}$  content in  $\text{TiO}_2$ . It is believed that the 2%  $\text{Bi}^{3+}$  ions are not all doped into  $\text{TiO}_2$ , and

parts of them have substituted the  $\text{Y}^{3+}$  ions in  $\text{YF}_3$ . The absorption edge of  $\text{TiO}_2$  may be enlarged by continuously increasing the  $\text{Bi}^{3+}$  contents (>2%), while the upconversion emission intensities, especially the UV and violet emissions will be decreased (Fig. S5d), and the optimal value of 2% is chosen thereafter.

### 3.3. NIR driven photocatalytic activities

The photocatalytic activities of the samples are measured under 980 nm NIR light irradiation (Fig. S6). As shown in Fig. 5a, ETYB-NYT exhibits better photocatalytic activity compared to ETY-NYT and ETY-NT. Based on the absorption edge (431 nm) of ETYB-NYT, the UV and violet emissions can directly excite  $\text{TiO}_2$ . To further utilize the strong blue and green emissions in the NIR driven photocatalytic experiment, a visible-light photocatalyst of  $\text{BiVO}_4/\text{CaF}_2: \text{Er}^{3+}, \text{Tm}^{3+}, \text{Yb}^{3+}$  (BVO/CF-1, prepared with pH 1) [4] with the band gap energy of 2.38 eV (Fig. S7) is added into the MO solution containing the ETYB-NYT samples (mass ratio of ETYB-NYT:BVO/CF-1 = 1:0.1), and the ETYB-NYT and BVO/CF-1 mixtures (Fig. S8) possess a higher degradation rate (10.33%) of MO compared to ETYB-NYT (7.54%).

The photocatalytic activities of the samples are also measured under NIR ( $\lambda \geq 780$  nm) light irradiation (Fig. S9). As shown in Fig. 5b, ETYB-NYT exhibits higher photodegradation rates (17.45%)

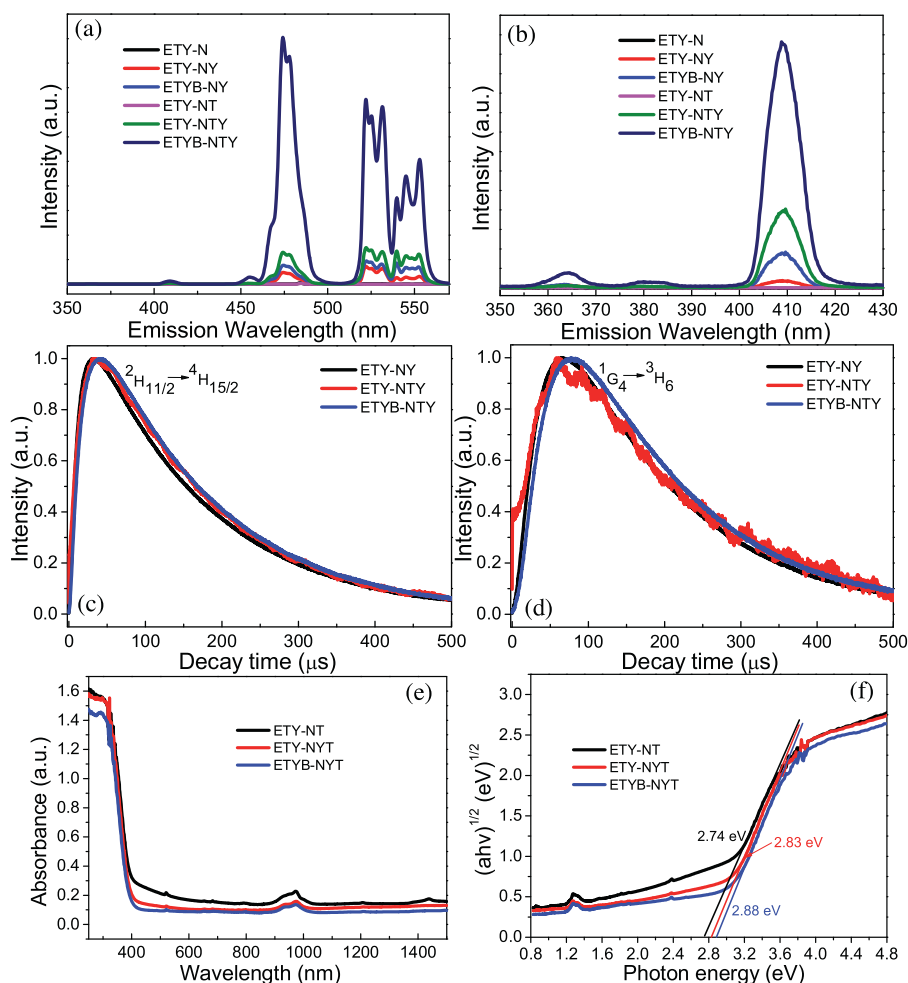


**Fig. 4.** (a and b) Upconversion luminescence spectra of ETY-N, ETY-NY, ETYB-NY, ETY-NT, ETY-NTY, and ETYB-NTY under 980 nm light excitation (output current = 3.0 A). Time-resolve fluorescence decay curves of the (c)  $^2H_{11/2}$  ( $Er^{3+}$ ) and (d)  $^1G_4$  ( $Tm^{3+}$ ) levels in ETY-NY, ETY-NTY, and ETYB-NTY, respectively. (e) UV-vis-NIR diffuse reflectance spectra and (f) the plots of the  $(\alpha hv)^{1/2}$  versus photon energy ( $h\nu$ ) for ETY-NT, ETY-NTY, and ETYB-NTY.

compared to ETY-NT (10.64%) and ETY-NTY (12.83%). It is a known fact that  $Yb^{3+}$  ions have a sufficient absorption band from 900 nm to 1000 nm [13], and the absorbed NIR light energy can be transferred to  $Er^{3+}$  and  $Tm^{3+}$  ions from  $Yb^{3+}$  ions to produce the red (658 nm), green (522 and 545 nm), blue (474 nm), violet (409 nm), and UV (364 and 380 nm) emissions (Fig. 6). From the UV and violet emissions of the samples (Fig. S4), it can be found that except for the absorption parts by  $TiO_2$ , ETYB-NTY still possesses stronger intensities compared to ETY-NTY and ETY-NT. The decay curves of the violet (409 nm,  $^2H_{9/2} \rightarrow ^4I_{15/2}$ ) and UV (364 nm,  $^1D_2 \rightarrow ^3H_6$ ) emissions are shown in Fig. 7a and b, respectively. The lifetimes of the  $^2H_{9/2}$  (160 μs) and  $^1D_2$  (151 μs) levels in ETYB-NTY are longer than those (150 and 149 μs) of ETY-NTY, which further demonstrate the higher upconversion efficiency of ETYB-NTY. Thus, based on the UV-vis-NIR absorption spectra (Fig. 4e and f), the best NIR driven photoactivity in ETYB-NTY is ascribed to its greatly improved UV and violet emissions (Fig. 6), which can produce higher yield of  $\cdot OH$  and  $O_2^{\cdot -}$  radicals (Fig. 5c–f) to destroy the MO molecules compared to ETY-NT and ETY-NTY.

According to the preparation method of ETYB-NTY,  $NaY(WO_4)_2$  precursors,  $Er^{3+}$ ,  $Tm^{3+}$ ,  $Yb^{3+}$ , and  $Bi^{3+}$  ions were added simultaneously before the introduction of TTIP and  $F^-$  ions. In the final obtained ETYB-NTY sample, the lanthanide ions ( $Er^{3+}$ ,  $Tm^{3+}$ , and  $Yb^{3+}$ ) can not only dope into  $YF_3$  crystals, but also exist in  $TiO_2$  coatings. Similar preparation method and the result with active-core/active-shell structure have been reported in our previous

work [14]. The enlarged UV-vis-NIR absorption spectra from 400 to 1200 nm are shown in Fig. S10, and several absorption peaks located at 488, 520, 653–683, 790, and 973 nm can be observed, which are assigned to the absorptions from the ground state  $^4I_{15/2}$  to the excitation states  $^4F_{7/2}$ ,  $^2H_{11/2}$ ,  $^4F_{9/2}$ ,  $^4I_{9/2}$ , and  $^4I_{11/2}$  of  $Er^{3+}$  ions, respectively. The peaks of 653–683 and 790 nm are also due to the  $^1G_4 \rightarrow ^3F_4$  and  $^3H_4 \rightarrow ^3H_6$  transitions of  $Tm^{3+}$  ions [15], respectively. The  $^2F_{5/2} \rightarrow ^2F_{7/2}$  transitions of  $Yb^{3+}$  ions can contribute to the 973 nm absorption as well. To compare these peaks, it can be found that the  $YF_3$ -free sample of ETY-NT possesses the highest absorption intensities, since that all the lanthanide ions added have been doped into  $TiO_2$ . Unlike ETY-NT, ETY-NTY and ETYB-NTY display lower absorption intensities, which are due to the fact that a part of the lanthanide ions have been taken by  $YF_3$ . On the other hand, this is the evidence that the  $TiO_2$  coatings of ETY-NTY and ETYB-NTY were all doped with lanthanide ions. Thus, the absorption peaks of 488, 520, 653–683, 790, and 973 nm from the lanthanide ions may also contribute to the improvement of photocatalytic activities [16], owing to the impurity states created by the lanthanide ions and  $Bi^{3+}$  ions in  $TiO_2$  [8,17,18].

### 3.4. UV-vis-NIR driven photocatalytic activities

The NIR photocatalysts are designed to utilize a broad spectrum light source or solar energy, and the UV-vis-NIR driven photocatalytic activities should be evaluated for the practical per-

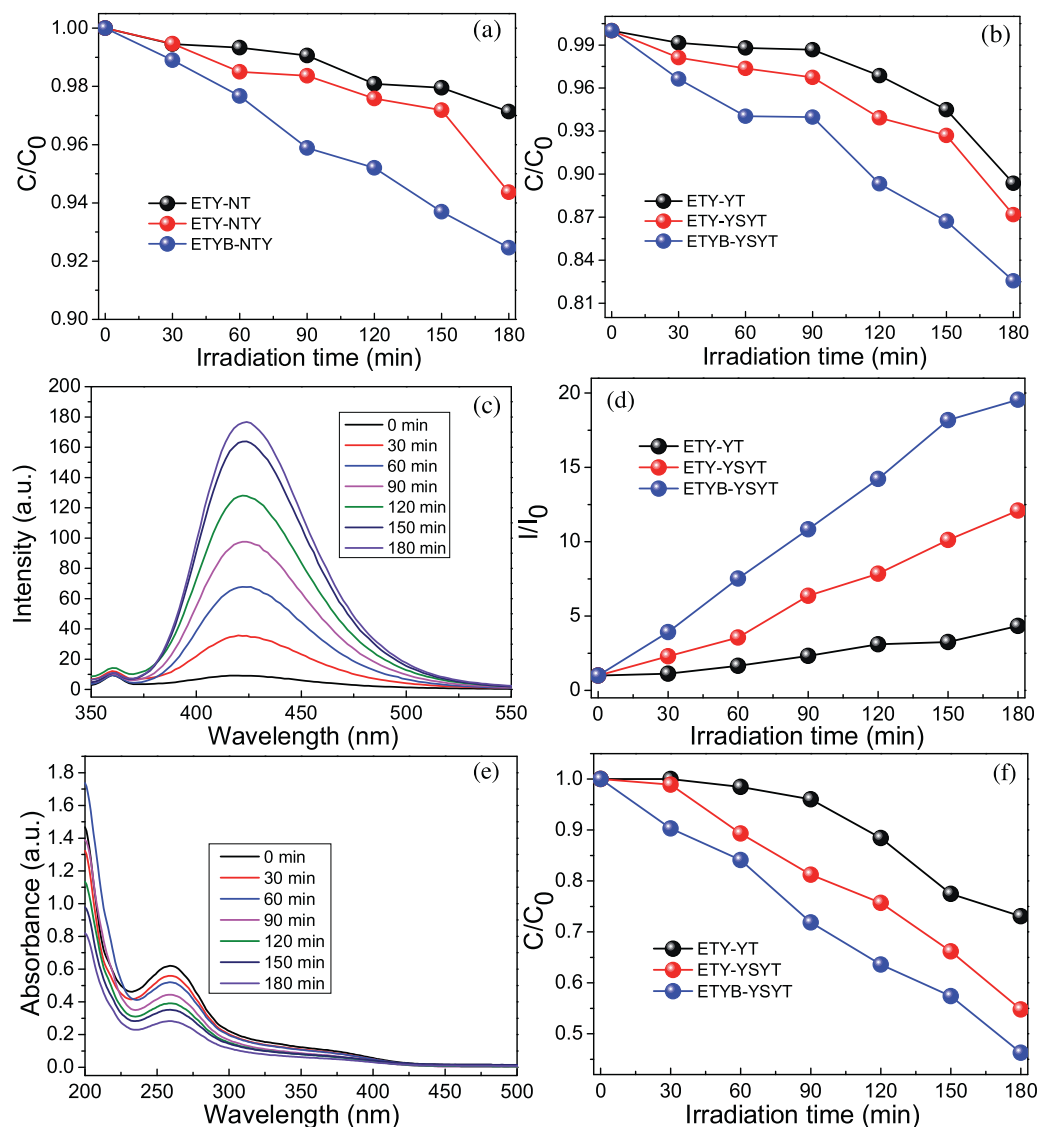


**Fig. 5.** (a)  $C/C_0$  conversion plots of MO for ETY-NT, ETY-NTY, and ETYB-NTY under 980 nm NIR light irradiation (output current = 2.0 A). (b)  $C/C_0$  conversion plots of MO for ETY-NT, ETY-NTY, and ETYB-NTY under NIR ( $\lambda \geq 780$  nm) light irradiation. (c) Time-dependent fluorescence spectra of the terephthalic acid solution over ETYB-NTY under NIR ( $\lambda \geq 780$  nm) light irradiation. (d) Photocatalytic activities of  $\cdot\text{OH}$  production over the samples under NIR ( $\lambda \geq 780$  nm) light irradiation. (e) Time-dependent absorption spectra of NBT over ETYB-NTY under NIR ( $\lambda \geq 780$  nm) light irradiation. (f) Photocatalytic activities of  $\text{O}_2^{\cdot-}$  production over the samples under NIR light ( $\lambda \geq 780$  nm) irradiation.

spective. Fig. 7c shows the photocatalytic decomposition of MO under UV-vis-NIR light irradiation, with the degradation rates of 87.44%, 92.90%, and 98.47% for ETY-NT, ETY-NTY, and ETYB-NTY, respectively. As for the colorless SA degradation (Fig. 7d), ETYB-NTY also possesses better photocatalytic activity (90.59%) compared to ETY-NT (64.70%) and ETY-NTY (81.43%). An additional photodegradation of SA over commercial Degussa P25 is present in Fig. S11, and its degradation rate (78.6%) is lower than that of ETYB-NTY. Compared to P25, the stronger degradation ability of ETYB-NTY is associated with its strong upconversion emissions and the efficient electron-hole pair separation (Fig. S12). The EEM fluorescence spectra of SA over ETYB-NTY as a function of irradiation time are shown in Fig. 8. It can be observed that the initial EEM fluorescence spectra (Fig. 8a) mainly include four regions [19]. Region I represents the aromatic-like compounds with the excitation/emission wavelengths (Ex/Em) of 210–230/290–340 nm. Region IV appears at Ex/Em = 250–290/290–340 nm are attributed to protein-like compounds, and region III at Ex/Em of 200–250/350–530 nm are related to fulvic acid-like compounds. Region V appears at Ex/Em = 250–350/350–530 nm can be attributed to humic-like

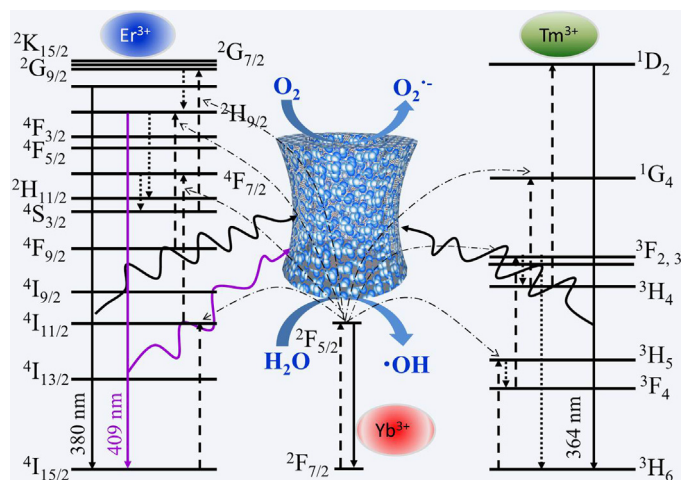


**Fig. 6.** Schematic energy-level diagrams of  $\text{Er}^{3+}$ ,  $\text{Tm}^{3+}$ , and  $\text{Yb}^{3+}$  ions and the energy transfer mechanisms among them under NIR excitation.



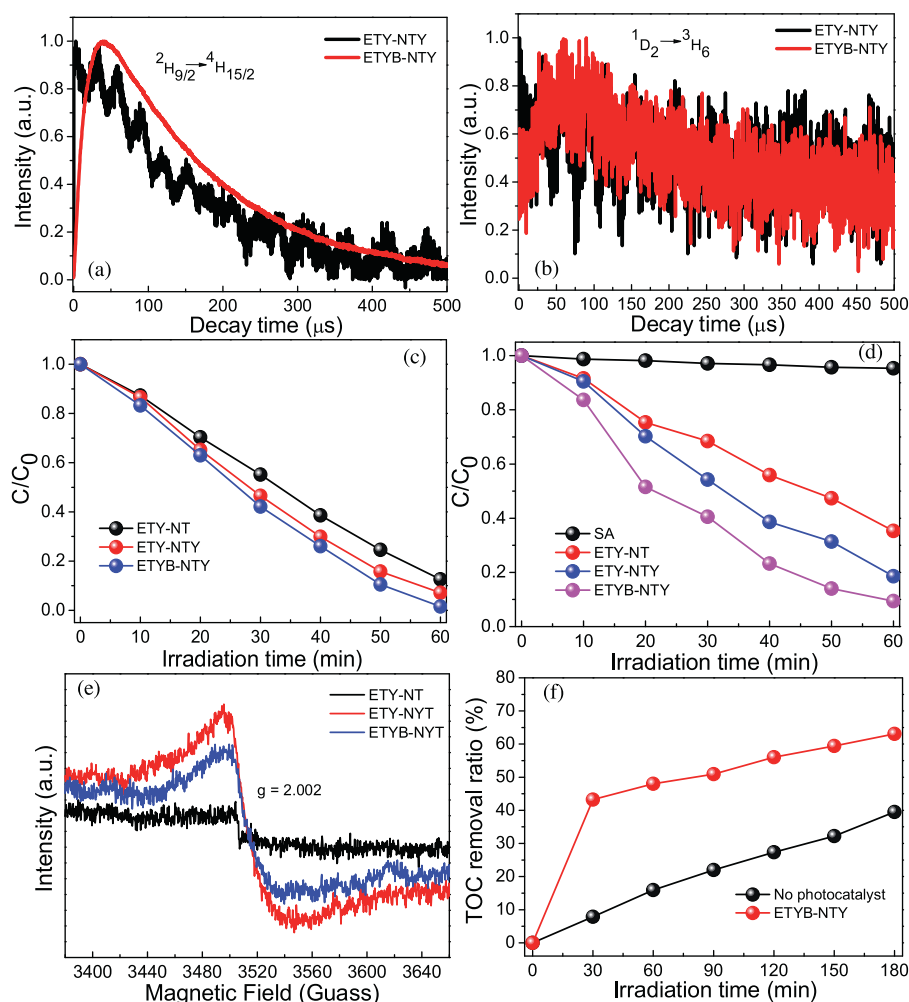


**Fig. 7.** Time-resolve fluorescence decay curves of the (a)  $^2H_{9/2}$  ( $Er^{3+}$ ) and (b)  $^1D_2$  ( $Tm^{3+}$ ) levels in ETY-NTY and ETYB-NTY, respectively.  $C/C_0$  conversion plots of (c) MO and (d) SA for ETY-NT, ETY-NTY, and ETYB-NTY under UV–vis–NIR light irradiation. (e) ESR spectra of ETY-NT, ETY-NTY, and ETYB-NTY. (f) TOC removal rates of leachate under UV–vis–NIR irradiation.

compounds. In the first degradation of 10 min, the fluorescence intensities of the four kinds of compounds are decreased greatly (Fig. 8b), and the aromatic-like compounds are almost disappeared. As the irradiation time extends to 40 min, most of fulvic acid-like and humic-like compounds are decomposed (Fig. 8c), and there is no significant difference in comparison to the obtained spectra after 60 min (Fig. 8d).

As expected, ETYB-NTY shows the best photocatalytic activities compared to ETY-NTY and ETY-NT, and it is mainly attributed to its much enhanced upconversion emission intensities. The PL emission intensity of ETYB-NTY is also lower than those of ETY-NTY and ETY-NT (Fig. S12), meaning the higher electron–hole pair separation efficiency for ETYB-NTY. Furthermore, ETY-NTY and ETYB-NTY both possess stronger ESR signal intensities compared to ETY-NT (Fig. 7e). The signal at  $g = 2.002$  is assigned to the single-electron-trapped oxygen vacancy (SETOV) [20,21], which can prevent the electron–hole pair recombination and improve the photocatalytic activity. As for ETYB-NTY, the ESR signal is slightly decreased compared to ETY-NTY, owing to its higher crystallinity by  $Bi^{3+}$  doping. However, in the photocatalytic processes, the great enhanced upconversion emission intensity and the higher photoinduced charge separation efficiency occupy the determining factors in ETYB-NTY, resulting in higher degradation rate than that of ETY-NTY.

To investigate the photodegradation ability of ETYB-NTY in the practical wastewater treatment, the leachate contained a large

amount of dissolved organic matter (DOM) was chosen. The initial EEM fluorescence spectra of the leachate are shown in Fig. 9a, and four fluorescence peaks (region II, III, IV, and V) are mainly observed before UV–vis–NIR irradiation. The fluorescence peaks of region II and IV are located at the emission wavelengths of 300–305 nm and 340–350 nm from the excitations of 275 and 225 nm, respectively, and they are ascribed to protein-like compounds, which are associated with the tryptophan and tyrosine, respectively [22,23]. Region III at Ex/Em of 230–250/420–450 nm is related to fulvic acid-like compounds, and region V at Ex/Em of 310–340/420–450 nm (aromatic and aliphatic groups in the DOM fraction) is attributed to humic-like compounds [24]. In the photocatalytic degradation process, there is a small degradation rate for the leachate with the strong UV light irradiation (Fig. 7f). However, a larger TOC removal rate of 43.27% is obtained over ETYB-NTY in the first 30 min. After that, stable degradation processes are present as the irradiation time extended. It can be inferred that the protein-like compounds in the leachate could be decomposed easily, since their fluorescence intensities decrease significantly in the initial 30 min (Fig. 9b). When the irradiation time increased to 120 min, few signals of the protein-like compounds can be detected (Fig. 9c). Unlike the protein-like compounds, the degradation of the fulvic acid-like and humic-like compounds needs a longer time (Fig. 9d). In comparison to SA (Fig. 8), the photodegradation process in the leachate is more complex, since the high concentration of  $Cl^-$  ions and other related substances contained in the leachate might quench the  $\cdot OH$  radicals

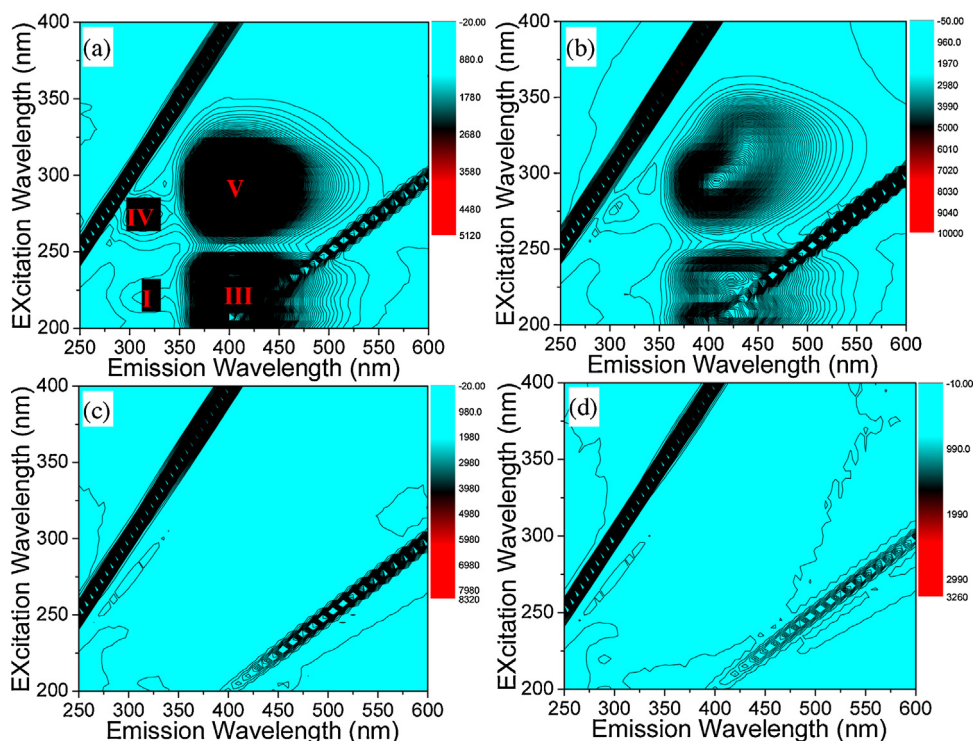


Fig. 8. EEM fluorescence spectra of SA under UV-vis-NIR irradiation over ETYB-NTY: (a) 0 min, (b) 10 min, (c) 40 min, and (d) 60 min.

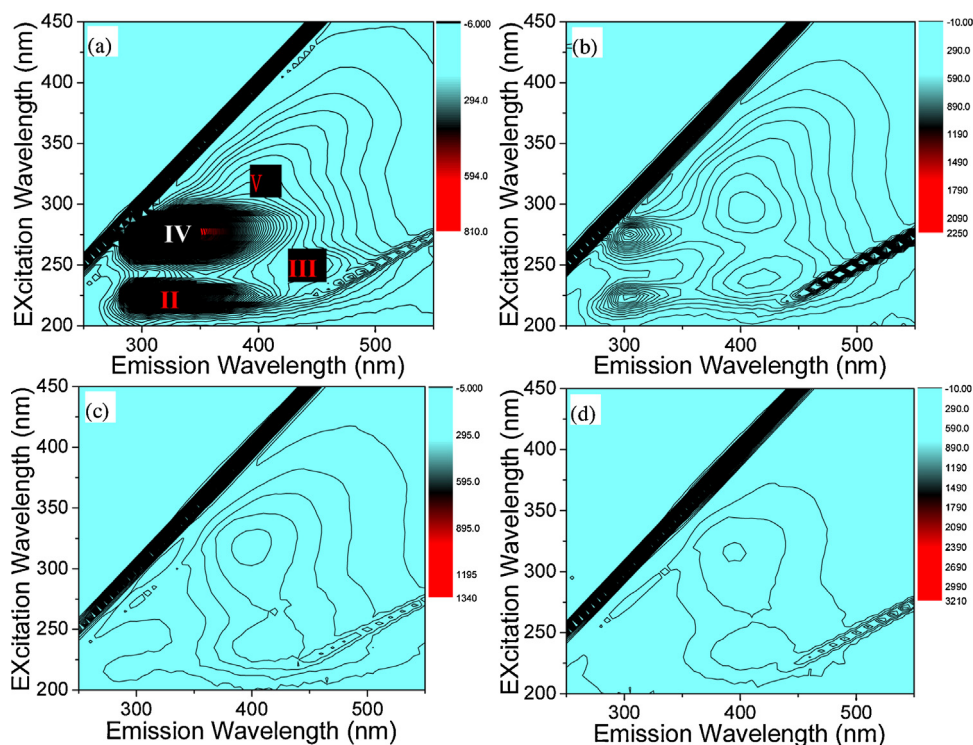


Fig. 9. EEM fluorescence spectra of the leachate under UV-vis-NIR irradiation over ETYB-NTY: (a) 0 min, (b) 30 min, (c) 120 min, and (d) 180 min.

during the photocatalytic processes [25]. However, the leachate is one of the most difficult disposal wastewater due to its complex components, and the photocatalytic activities can be accepted based on the results. Thus, the NIR photocatalyst of ETYB-NTY has potential application in the pretreatment of the leachate and other wastewater.

#### 4. Conclusions

A novel NIR photocatalysts of ETYB-NTY was synthesized by a multi-stage formation method.  $\text{NaY}(\text{WO}_4)_2$  was used as the precursor to slowly release  $\text{Y}^{3+}$  ions, and the  $\text{YF}_3$  upconversion agent and  $\text{TiO}_2$  semiconductor were formed and deposited continuously on



the surfaces of the remaining  $\text{NaY}(\text{WO}_4)_2$ . ETY-NTY displays higher upconversion emission intensity compared to ETY-N, ETY-NY, ETYB-NY, and ETY-NT, and a dramatic improvement of upconversion is further obtained in ETYB-NTY by  $\text{Bi}^{3+}$  doping, which provides better NIR driven photocatalytic activity for ETYB-NTY compared to ETY-NT and ETY-NTY. Under UV–vis–NIR irradiation, ETYB-NTY also shows higher degradation rates in decomposition of MO and SA. For the leachate, it is easier to remove the protein-like compounds compared to the fulvic acid-like and humic-like compounds over the ETYB-NTY system.

### Acknowledgement

This work was supported by the Science and Technology Commission of Shanghai Municipality (no. 14DZ1207306), the Shanghai Rising-Star Program (no. 14QA1402400), the National Key Technology R and D Program (no. 2014BAL02B03-4), and Shanghai Tongji Gao Tingyao Environmental Science and Technology Development Foundation.

### Appendix A. Supplementary data

Supplementary data associated with this article can be found, in the online version, at <http://dx.doi.org/10.1016/j.apcatb.2014.12.039>.

### References

- [1] D.X. Xu, Z.W. Lian, M.L. Fu, B.L. Yuan, J.W. Shi, H.J. Cui, *Appl. Catal. B* 142–143 (2013) 377–386.
- [2] W.P. Qin, D.S. Zhang, D. Zhao, L.L. Wang, K.Z. Zheng, *Chem. Commun.* 46 (2010) 2304–2306.
- [3] G.B. Shan, G.P. Demopoulos, *Adv. Mater.* 22 (2010) 4373–4377.
- [4] S.Q. Huang, N.W. Zhu, Z.Y. Lou, L. Gu, C. Miao, H.P. Yuan, A.D. Shan, *Nanoscale* 6 (2014) 1362–1368.
- [5] S. Xu, W. Xu, Y.F. Wang, S. Zhang, Y.S. Zhu, L. Tao, L. Xia, P.W. Zhou, H.W. Song, *Nanoscale* 6 (2014) 5859–5870.
- [6] S.Q. Huang, Z.Y. Lou, A.D. Shan, N.W. Zhu, K.L. Feng, H.P. Yuan, *J. Mater. Chem. A* 2 (2014) 16165–16174.
- [7] N. Niu, F. He, S.L. Gai, C.X. Li, X. Zhang, S.H. Huang, P.P. Yang, *J. Mater. Chem.* 22 (2012) 21613–21623.
- [8] A. Hamdi, A.M. Ferraria, A.M. Botelho do Rego, D.P. Ferreira, D.S. Conceição, L.F. Vieira Ferreira, S. Bouattour, *J. Mol. Catal. A-Chem.* 380 (2013) 34–42.
- [9] Q. Lü, L.C. Zhao, F.Y. Guo, M.C. Li, *Chin. Phys. B* 18 (2009) 4030–4036.
- [10] X.Y. Guo, W.Y. Song, C.F. Chen, W.H. Di, W.P. Qin, *Phys. Chem. Chem. Phys.* 15 (2013) 14681–14688.
- [11] H. Qiu, C. Yang, W. Shao, J. Damasco, X. Wang, H. Agren, P.N. Prasad, G. Chen, *Nanomaterials* 4 (2014) 55–68.
- [12] G. Chen, H. Liu, H. Liang, G. Somesfalean, Z. Zhang, *J. Phys. Chem. C* 112 (2008) 12030–12036.
- [13] C. Cascales, M.D. Serrano, F. Esteban-Betegón, C. Zaldo, R. Peters, K. Petermann, G. Huber, L. Ackermann, D. Rytz, C. Dupré, M. Rico, J. Liu, U. Griebner, V. Petrov, *Phys. Rev. B* 74 (2006) 174114.
- [14] S.Q. Huang, L. Gu, C. Miao, Z.Y. Lou, N.W. Zhu, H.P. Yuan, A.D. Shan, *J. Mater. Chem. A* 1 (2013) 7874–7879.
- [15] W. Xu, J.P. Denis, G. Özen, A. Kermaoui, F. Pellé, B. Blanzat, *J. Appl. Phys.* 75 (1994) 4180–4188.
- [16] Z.J. Zhang, W.Z. Wang, Y. Zhou, *Appl. Surf. Sci.* 319 (2014) 250–255.
- [17] J. Reszczyńska, T. Grzyb, J.W. Sobczak, W. Lisowski, M. Gazda, B. Ohtani, A. Zaleska, *Appl. Catal. B* 163 (2015) 40–49.
- [18] S. Obregón, A. Kubacka, M. Fernández-García, G. Colón, *J. Catal.* 299 (2013) 298–306.
- [19] W. Chen, P. Westerhoff, J.A. Leenheer, K. Booksh, *Environ. Sci. Technol.* 37 (2003) 5701–5710.
- [20] Y. Wang, C.X. Feng, M. Zhang, J.J. Yang, Z.J. Zhang, *Appl. Catal. B* 104 (2011) 268–274.
- [21] X.L. Yu, Y. Wang, X.J. Meng, J.J. Yang, *Chin. J. Catal.* 34 (2013) 1418–1428.
- [22] P.G. Coble, *Mar. Chem.* 51 (1996) 325–346.
- [23] B.D. Xi, X.S. He, Z.M. Wei, Y.H. Jiang, D. Li, H.W. Pan, H.L. Liu, *Ecotox. Environ. Saf.* 86 (2012) 227–232.
- [24] S.L. Huo, B.D. Xi, H.C. Yu, H.L. Liu, *Water Environ. J.* 23 (2009) 15–22.
- [25] C.H. Liao, S.F. Kang, F.A. Wu, *Chemosphere* 44 (2001) 1193–1200.